Directly Deposited Thin-Film Strain Gauges for Force Measurement at Guide Carriages

Rico Ottermann, Dennis Kowalke, Berend Denkena, Michael Korbacher, Matthias Müller, and Marc Christopher Wurz

***Abstract*—Many industrial production processes use sensors to generate information about the manufacturing process. In this way, monitoring machine tools ensures the proper functionality of the system and detects unexpected behavior due to, for example, material inhomogeneity, incorrect data input, temperature influence, or tool wear. In large production machines, such as portal milling machines, the sensor equipment of guide carriages can be an important possibility since they are a standardized component and can be easily integrated into existing machines. Here, conventional polymer foil-based strain gauges show several disadvantages due to reproducibility and reliability of the sensor connection via adhesive. Thus, this article addresses the manufacturing of directly deposited chromium thin-film strain gauges on a guide carriage with integrated programmable data preamplification. Tests with different sensor materials on steel substrates showed that chromium was the most suitable sensor material with a high *k*-factor. Then, one end face of the carriage was polished before sputtering an Al_2O_3 insulation layer and a chromium sensor layer that was laser-structured afterward to produce two Wheatstone full bridges at previously simulated sensor positions. In a tensile test stand, the calibration of the sensors took place in the two spatial directions perpendicular to the guide rail direction. With an additional sensor data fusion for the final interpretation of measured forces, it is shown that this sensor technology is suitable for force measurement at guide carriages.**

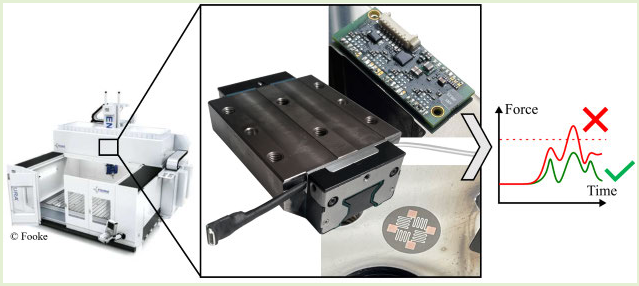

***Index Terms*— Condition monitoring, direct deposition, force measurement, guide carriages, *K*-factor, machine tool, sensor integration, strain gauges, temperature coefficient of resistance (TCR), thin-film sensors.**

I. Introduction

THE aim of intelligent and autonomous industrial production drives the development and integration of sensors for manufacturing processes. Sensor data can be used for condition monitoring and error detection on the one hand and as input for automatic control on the other hand.

This article addresses the sensory equipment of portal milling machines, particularly sensory guide carriages (see Fig. 1). Conventional guide carriages are standardized machine components. This offers the possibility to exchange selected guide carriages for the integration of sensory guide carriages into existing systems. This approach can be found for several machine elements such as bearings, screws, couplings, seal rings, shafts, or gears [1].

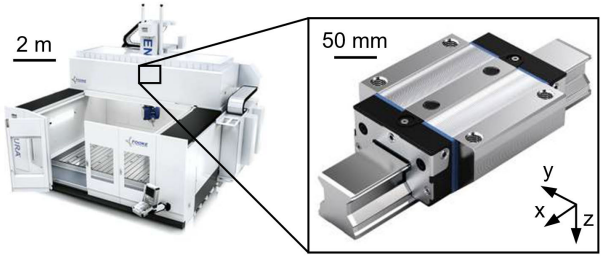

Fig. 1. Portal milling machine from Fooke [2] and guide carriage with guide rail from Bosch Rexroth [3].

Received 26 August 2024; accepted 9 October 2024. Date of publication 17 October 2024; date of current version 13 December 2024. This work was supported by German Research Foundation (DFG) through the Research Project "Force-Sensitive Guide Systems Based on Directly Deposited Component-Specific Sensors" under Project 428561441. The associate editor coordinating the review of this article and approving it for publication was Prof. Tao Li. *(Corresponding author: Rico Ottermann.)*

Rico Ottermann is with the Micro and Nano Integration Department, Institute of Micro Production Technology, Leibniz University Hannover, 30823 Garbsen, Germany (e-mail: ottermann@impt.uni-hannover.de).

Dennis Kowalke and Berend Denkena are with the Institute of Production Engineering and Machine Tools, Leibniz University Hannover, 30823 Garbsen, Germany (e-mail: kowalke@ifw.uni-hannover.de; denkena@ifw.uni-hannover.de).

Michael Korbacher is with the Research and Development Department, Bosch Rexroth AG, 97424 Schweinfurt, Germany (e-mail: michael.korbacher2@boschrexroth.de).

Matthias Müller is with the Research and Development Department, Fooke GmbH, 46325 Borken, Germany (e-mail: mmueller@fooke.de).

Marc Christopher Wurz is with the Institute of Micro Production Technology, Leibniz University Hannover, 30823 Garbsen, Germany (e-mail: wurz@impt.uni-hannover.de).

Digital Object Identifier 10.1109/JSEN.2024.3478821

To enable an intelligent guide carriage, conventional polymer-foil-based strain gauges can be used, which are attached via adhesive [4], [5], [6]. Because of the viscoelastic adhesive and the polymer substrate foil thickness, errors in application can lead to low reproducibility, reduced reliability, or even complete sensor failure due to detachment [7], [8]. This is where directly deposited sputtered thin-film sensors have advantages. They can have higher sensitivity, reduced space requirements, improved temperature behavior and long-term stability, as well as faster dynamic response [9], [10], [11], [12], [13].

In this article, the advantages of directly deposited thin-film strain gauges are used on guide carriages to measure extremely low strain values in the range below 1 μm/m. Therefore, a suitable sensor material with an increased strain sensitivity has to be found, indicated by the k-factor.

Here, different materials can be found in the literature. Conventional materials, such as Constantan (CuNiMn) and nickel–chromium (NiCr), show k-factors of around 2 [14]. Compounds with silver have higher values, such as Ni35Ag65 with maximum k-factors of 2.5 [15] or Ag-ITO (indium–tin oxide) with the highest k-factor of 7 if the Ag content is 20 at% [16], [17]. ITO coatings itself can have a k-factor of 5.3 [18].

Pure metals, such as platinum and titanium, reveal a k-factor of 3.8–4.5 [19], [20] and 3.8 [21]. For gold, depending on the surface resistivity, k-factors up to 5 are documented for low resistivities or even up to 170 for high-resistivity Au thin film with high defect rates and high roughness [22]. Another alloy, Invar36 (Ni-Fe alloy), shows strain sensitivities in the range of 2.5–4.5 depending on the film thickness [23]. Sensor materials, such as $TiAlN_xO_y$ and AlN5Pt5, have k-factors around 2.5 [24] and 4.7 [25]. Alloys with nitrogen often have an increased strain sensitivity: a value between 3.4 and 6.2 is documented for TaN [26], [27]. AlN_x has k-factors up to 15 [28]. For TiN, values up to 7 are recorded [29]. Niwa et al. [30], Niwa and Hiroshi [31], and Niwa et al. [32] developed CrN strain gauges with k-factors between 8 and 16. For other materials such as CrO_xSi_y, k-factors of 5.2–10.3 were found for films with maximal values below 5 at% Si [33]. Multilayer coatings of Pt/SiO_2 show k-factors up to 18 [34].

In general, semiconductor materials have higher k-factors because the strain sensitivity is not only caused by the geometrical change but also especially due to a strain-induced change of the conductivity itself [35]. This can be seen in (1), which describes the k-factor k in relation to Poisson's ratio ν, the resistivity ρ, and the elongation ε

$$k = (1 + 2 \cdot \nu) + (\Delta\rho/(\rho \cdot \varepsilon)). \tag{1}$$

Here, the term $1 + 2{\cdot}\nu$ represents the geometrical change and $\Delta\rho/(\rho \cdot \varepsilon)$ stands for the strain-induced resistivity change [14]. The high piezoresistive effect is a consequence of the fact that semiconductors possess load carriers (e.g., electrons) in both the valence band and the conduction band. The mobility of these load carriers is influenced by mechanical elongation, as the isotropic behavior of the lattice structure is affected by the distortion of the lattice structure [36]. That is the reason why research often focuses on the addition of elements such as O, N, or C to metals to achieve semiconductor properties. A thin-film material that has already been tested on guide carriages up to 100 kN is diamond-like carbon (DLC) [37], [38], [39], [40]. These coatings have high resistivities and can reach k-factors of 64 [37] or even up to 1200 [41], [42]. Since DLC coatings have high-temperature dependency, different metal components (e.g., W, Ti, and Ni) were investigated as alloy partners [16]. Here, k-factors over 10 were achieved for Ni-DLC.

The most typical semiconductor strain gauge material is silicon that can have k-factors up to 200 for p-type (110) single crystalline silicon [43], [44], [45]. For p-type polycrystalline silicon, values up to 25 [35] or even up to 34 [46], [47] were measured.

Since most of these mentioned materials have their disadvantages when they should be used on guide carriages due to insufficient k-factors, temperature behavior, thin-film manufacturing and structuring methods, reproducibility, and price, this article addresses the material selection for the sensor layer, including their characterization. Therefore, typical metals should be tested, which have comparingly low-temperature coefficients. For some of them, no literature values can be found or only bulk material values are available. A slight doping with oxygen or nitrogen could lead to the desired effect of high strain sensitivity, while the resistivity remains in a range that can be easily utilized for the production of strain gauges. In combination with an FEM-based simulation of suitable sensor positions and alignments, the sputter deposition and laser structuring of thin films on the guide carriage is shown. Finally, the integration of a PCB board for data preamplification is presented for the static calibration and testing of the sensors in a tensile test stand.

II. Simulation

Other methods to measure plane strain on metallic bodies using strain gauges often use limb structures or spoke components and optimize the geometries to increase the strains occurring so that strain gauges with conventional sensitivity can be used [48], [49], [50], [51], [52], [53], [54]. Since this is directly affecting the stiffness of the metal component, it can only be used for external strain transducers that are attached to the measurement object. In contrast, the approach presented in this article is to maintain the stiffness of the measurement object, the guide carriage, which is necessary for usage in high-precision milling machines [54]. In addition, the standardized geometry of the guide carriage should not be changed to enable the replacing of sensory guide carriages in machines without any change in the mechanical properties. On the one hand, this is the reason for the need of a sensor material with a high strain sensitivity. On the other hand, suitable sensor positions should increase the sensor signal.

Therefore, the number of sensors, their positions, and alignments have to be determined via simulations. The aim is to develop a sensor layout that is able to address the conflict of objectives between maximum sensitivity, providing information about different forces, simple evaluation for industrial use, and the feasibility and reasonable effort of thin-film sensor production.

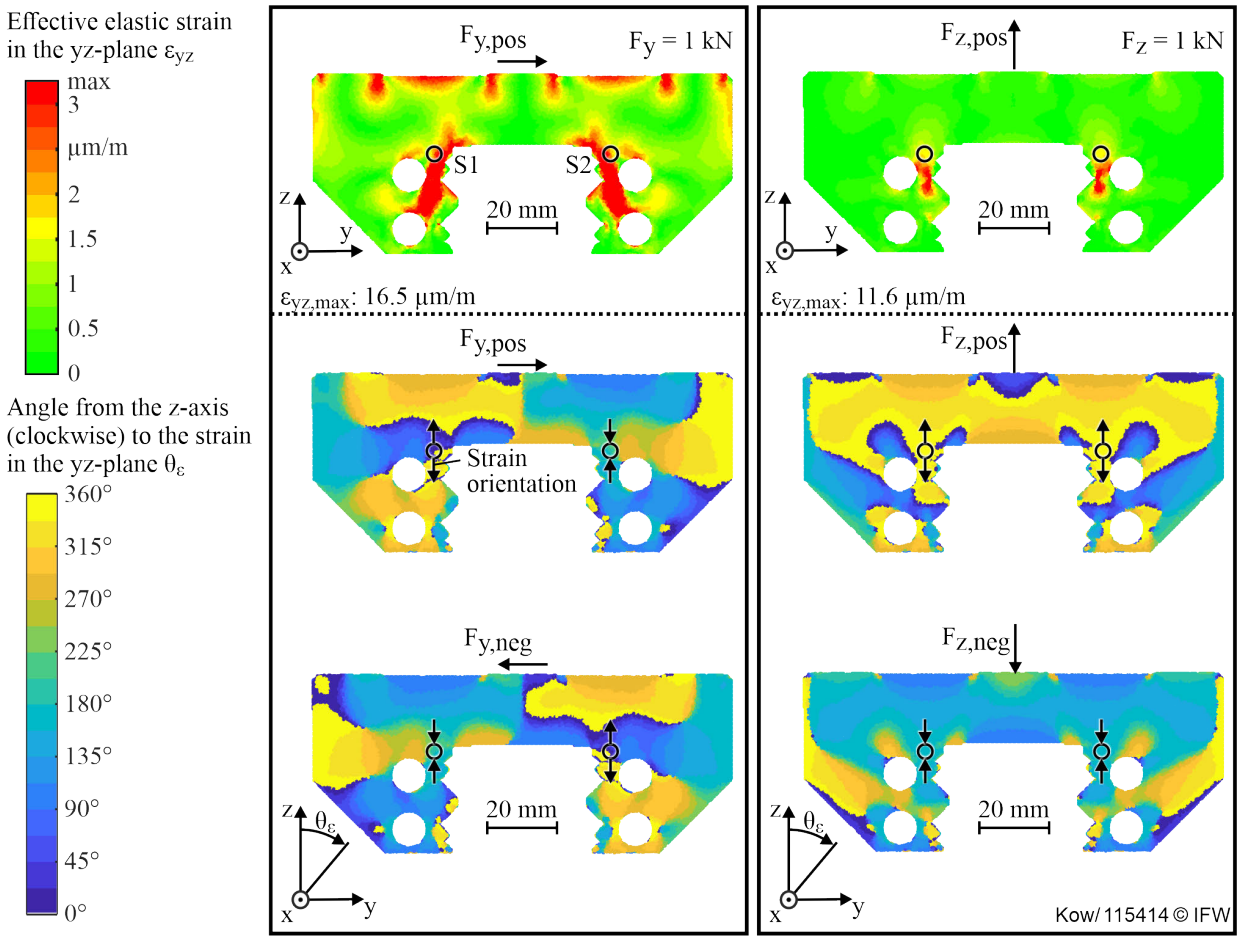

Fig. 2. FEM simulation results on the end face of a guide carriage with load introduction in the *y*- and *z*-directions.

The most important measurands are the forces in the *y*- and *z*-directions, which are the two spatial directions perpendicular to the direction of the guide rail on which the carriage runs, as shown in Fig. 2 (compare Fig. 1). The measurement of momentums only plays a minor role since the carriages are always used in a compound.

To identify positions for sensors, an FEM-based simulation was conducted. In order to investigate the relationship between external forces and surface strain, the simulation was conducted using a reference force of 1 kN for each direction. The reference force is comparable to the forces of a misaligned rail [5] or a milling process [55]. The force engages the guide carriage on the mounting faces on the top side and the mounting threads. To account for the behavior of a mounted guide carriage, an analogous component was defined on the top side of the guide carriage. This component imitates the stiffness and its reduction of the guide carriage deformation. The boundary conditions for the simulation of the guide carriage contact with the rail were selected for a stationary guide carriage. During standstill, the rolling elements inside the guide carriage responsible for the contact between the guide rail and the guide carriage do not change their position. Nevertheless, different rolling element positions must be taken into account for the simulation. Because of influences such as friction, load, and lubrication, the relative position of the rolling elements to each other changes during the guide carriage motion. The individual contact for each rolling element is simulated using a single spring element. The area on which the spring operates is calculated in accordance with Hertz's contact theory. The force of the spring elements is based on an approximation by Kunert [56] and verified based on the displacement under load as stated in the datasheet of the guide carriage. The simulation was carried out with the reference force for the *y*-axis and *z*-axis, taking into account the positive and negative directions.

The simulation results for the effective elastic strain in the surface plane and the strain orientation are shown for different loads in Fig. 2. The simulation results for the effective elastic strain from loads in the negative direction are comparable to the strain from loads in the positive direction. The simulation shows the effective elastic strain values of up to $\varepsilon_{yz} = 16.5\ \mu$m/m and $\varepsilon_{yz} = 11.6\ \mu$m/m, respectively, for loads of 1 kN in the *y*- or *z*-direction. The effective elastic strain is calculated as the Pythagorean sum of the elastic strain in *y*- and *z*-directions. Since the effective elastic strain does not contain information regarding the strain's orientation, the strain vector's angle is calculated for the identification of a suitable sensor orientation. Since the high strain values occur at positions where sensor positioning is not feasible (the area between the boreholes and the raceways), the two sensor positions (left: Sensor S1 and right: Sensor S2) indicated by the black circles are chosen. The scale does not show the complete strain range up to 16.5 μm/m to ensure

TABLE I
EXPECTED SENSOR SIGNALS FOR STRAIN GAUGES AT THE TWO POSITIONS INDICATED IN FIG. 2 WITH THE CORRESPONDING PRIMARY STRAIN ANGLES

Load	Left position		Right position	
	Sensor signal	Strain angle	Sensor signal	Strain angle
y-direction compression	Positive	0°	Negative	180°
y-direction elongation	Negative	180°	Positive	0°
z-direction compression	Positive	0°	Positive	0°
z-direction elongation	Negative	180°	Negative	180°

high resolution in the lower strain region, especially between 0 and 3 μm/m. The position of the black circles offers a compromise for the conflict of objectives concerning high and homogeneous strain values, distinguishability of the different load scenarios and manufacturability with sputter deposition, as well as integration possibility into the housing of the guide carriage. At these positions, strain values are between 0.5 and 2 μm/m.

The distinguishability of the different load scenarios is given at the selected positions due to orientational changes for the different scenarios. For example, with loads in the z-direction, the strain orientation at both sensor positions is identical and changes by 180° between positive and negative loads leading to corresponding positive (0°) or negative (180°) sensor signals. For loads in the y-direction, both sensor positions show contrary strain orientations. For a change in the load direction at both sensor positions, the strain direction changes by 180°. The change of the orientation by 180° means that compressive strain becomes elongation strain and vice versa. Therefore, a change in the sensor signal sign is expected. The different orientations of the strain for different loads and their influence on the signal of the strain gauges allow for distinguishing between the four different load cases. The observation of both sensor positions results in a clear assignment of the load introduction, as summarized in Table I. The angle of the primary strains occurring is also included and shows how the strain gauges should be oriented. Since a symmetrical full bridge is to be used later, differences in steps of 90° in the strain direction can be measured equally well. As only angles of 0° and 180° occur according to Table I, there is no conflict of objectives with regard to the alignment of the sensors for measuring the strains in both the y- and z-directions.

To account for the different positions of the rolling elements, an additional simulation was conducted, in which rows of the rolling elements were offset. This shows that the position of the rolling element influences the surface strain at a constant load. The results indicate that there is no set of positions without any influence of the rolling elements while also showing an influence from the loads. The minimal achievable force uncertainty F_{min} based on a few assumptions (SNR = 3) can be calculated according to (2) [55]. Here, Δf represents the frequency range (333 Hz, quasi-static), k_{B} is Boltzmann's constant, T is the temperature (298.15 K), R is the strain gauge initial resistance (350 Ω), e_{VR} is the noise voltage density (33 nV/$\sqrt{\mathrm{Hz}}$), U_{Ref} is the reference voltage (5 V), k is the k-factor, B stands for the bridge factor (2.6 for full-bridges), and S_{Mech} represents the mechanical sensitivity

$$F_{\mathrm{min}} = 24 \cdot \sqrt{\left(\Delta f \cdot \left(4 \cdot k_{\mathrm{B}} \cdot T \cdot R + e_{\mathrm{VR}}^2\right)\right)} / (U_{\mathrm{Ref}} \cdot k \cdot B \cdot S_{\mathrm{Mech}}). \quad (2)$$

Conventional strain gauge materials, such as Constantan or NiCr, have a strain sensitivity (k-factor) of around 2 [14]. Consequently, a force uncertainty of about 563 N would result, which would not fulfill the requirements to enable sufficient process control. Therefore, Section III-B addresses the development of high-sensitive thin-film strain gauges. For the desired force uncertainty in the range of 100 N, a k-factor of at least 10 is needed. Because of these high requirements, directly deposited thin-film sensors seem appropriate since they measure directly on the component's surface. Therefore, in Section III-B, different sensor layer materials are tested to find a suitable strain gauge material.

III. MATERIAL SELECTION AND LAYER DEVELOPMENT

A. Insulation Layer

1) Manufacturing of the Insulation Layer: In the context of industrial production processes, measurement objects are mostly metallic, which results in the necessity of an insulation layer between the measurement object and the sensor layer. Conventional polymer foil-based strain gauges use a polymer foil as substrate material, which also serves as the insulation layer. Thin-film strain gauges use the deposition of a ceramic insulation layer [57].

Due to the size of the guide carriage type RWD-045-FLS-CS-C3-U-DS-0-02-00-00-BX-LS-LSS-RS-LSS-01 from Bosch Rexroth with outer dimensions of approximately 134 × 120 × 53 mm, the sputter coating system Z550 from Senvac is used for the deposition as it provides the required space inside the coating chamber.

Previous work with other coating systems showed that a thin-film insulation layer of alumina (Al_2O_3) is suitable for use on steel surfaces [8], [10], [58], [59]. Here, roughness plays a major role in providing sufficient insulation properties [10]. In addition, the characteristics of the insulation layer can be improved through cleaning steps between the insulation layer deposition [58]. The main properties of a thin-film insulation layer include adhesion, stoichiometry, resistivity, and the breakdown field strength. In addition, the yield is essential. Because the sputtering parameters influence the thin-film characteristics, they were investigated first. The sputtering power was kept constant at 400 W (a power density of 24.2 W/cm^2 and a target diameter of 16.51 cm) and the sputtering time was set to 10 h. Based on [10], [60], and [61], six different sputtering gas combinations according to Table II were tested.

Here, 3-sccm O_2 was the minimum possible value, limited due to the corresponding mass flow controller of the sputtering system. In order to achieve common sputtering pressure values based on previous results [60] and known from the literature [61], the corresponding Ar gas flows were used. As substrate material, polished stainless-steel wafers (1.4301) with a diameter of 100 mm and a thickness of 0.8 mm,

TABLE II
PARAMETERS FOR ALUMINA DEPOSITION

Number	1	2	3	4	5	6
Ar (sccm)	59	56	40	37	78	75
O_2 (sccm)	0	3	0	3	0	3
O_2/Ar (%)	0	5.4	0	8.1	0	4
Sputter pressure (10^{-3} mbar)	9.0	9.0	5.8	5.8	11.8	11.8
Sputter rate (nm/min)	17.7 ± 1.3	10.7 ± 1.2	19.8 ± 2.5	8.1 ± 1.9	17.6 ± 3.1	9.7 ± 1.5
Thickness (µm)	10.6 ± 0.8	6.4 ± 0.7	11.9 ± 1.5	4.9 ± 1.1	10.6 ± 1.9	5.8 ± 0.9

TABLE III
RESISTIVITY, THICKNESS, AND STOICHIOMETRY FOR ALUMINA THIN FILMS DEPOSITED WITH DIFFERENT PARAMETERS ACCORDING TO TABLE II

Nr.	Resistivity (Ωcm)	Thickness (µm)	Stoichiometry (Al:O)	Yield (%)
1	$7.1 \cdot 10^{14} \pm 2.8 \cdot 10^{14}$	10.6	45:55 ± 1	91
2	$1.4 \cdot 10^{8} \pm 9.8 \cdot 10^{7}$	6.4	42:58 ± 2	17
3	$1.1 \cdot 10^{14} \pm 8.8 \cdot 10^{13}$	11.9	44:56 ± 1	86
4	$5.6 \cdot 10^{12} \pm 4.1 \cdot 10^{12}$	4.9	39:61 ± 1	59
5	$6.9 \cdot 10^{13} \pm 6.9 \cdot 10^{13}$	10.5	47:53 ± 3	86
6	$5.7 \cdot 10^{11} \pm 5.4 \cdot 10^{11}$	5.8	39:61 ± 1	45

were used. The mean roughness R_a and the mean roughness depth R_z were 13 ± 4 nm and 144 ± 73 nm, measured with the tactile surface roughness tester Hommel-Etamic W5 from Jenoptik. The tip radius of the measurement needle was 2 µm, and the measuring length was 4.8 mm. For the electrical characterization of the insulation layer, metal contact pads were sputter-coated to serve as upper electrodes, whereas the substrate represents the lower electrode. The measurement of the layer height took place with the white-light interferometer WYKO and the tactile measurement machine Dektak^{3}ST from Veeco. Basically, a major influence can be seen depending on the presence of oxygen. The film thickness was approximately 11 µm for numbers 1, 3, and 5 without any oxygen, and approximately 6 µm for numbers 2, 4, and 6 with oxygen. The sputtering rate was in the range of 18 nm/min for depositions without oxygen (1, 3, 5) and 9 nm/min when oxygen was present.

2) Characterization of the Insulation Layer: The different sputter conditions led to different stoichiometry in the coating, as shown in Table III. The measurements took place in a scanning electron microscope (SEM)-type LEO 1455VP with energy-dispersive spectroscopy (EDS) from Oxford. Three measurements on different diameters were done per sample. The mean values show that without the presence of oxygen gas, the oxygen content in the thin-film layer is too low compared to the reference value for perfect stoichiometry (Al_2O_3, Al:O = 40:60). The resistivity of the films was measured with the Ohm and Current Meter TO 3 from FISCHER with a measurement voltage of 30 V. In contrast to the stoichiometry results, the films without oxygen as additional sputtering gas revealed higher resistivity values, as shown in Table III. They are comparable to literature values ranging around 1×10^{14} Ω·cm [62]. Measurement results for contact pads resulting in resistance values below 1 kΩ were excluded from the calculation of the mean value for the resistivity. Therefore, Table III gives the information about the yield. For the depositions without oxygen (numbers 1, 3, and 5), the yield was in the range of 80% or 90%. Samples sputtered with oxygen show a lower yield, approximately between 20% and 60%. One reason for this behavior can be attributed to the different layer thicknesses.

For the evaluation of the breakdown field strength, another stainless-steel wafer was processed with an alumina layer thickness of approximately 2 µm. This was necessary to achieve breakthroughs within the maximum voltage of 500 V of the Ohm and Current Meter TO 3. For manufacturing, the parameters for the highest resistivity values (number 1) were used. The result was a mean value of 1.3 ± 0.1 MV/cm, which is comparable to literature values in the range of 1.5 MV/cm [63]. For the evaluation of the adhesion strength, tape tests were done. No differences could be observed for different alumina depositions. Minimum values of 10 MPa were achieved, which is in agreement with [8].

B. Sensor Layer

1) Manufacturing of the Sensor Layer: As the FEM simulation results showed, common materials, such as Constantan, are not suitable for the desired application since they offer a k-factor of 2, which is too low. The first improvement is the use of Wheatstone full-bridges as they offer a gain in sensitivity compared to single quarter-bridges of $2 \cdot (1 + \nu)$. Here, ν is Poisson's ratio. To overcome still remaining sensitivity restrictions, a detailed material analysis with various metal thin films concerning the k-factor and temperature coefficient of resistance (TCR) is performed. These materials are Constantan (Cu54Ni45Mn1), NiCr (50:50 wt%, 60:40 wt%, and 80:20 wt%), titanium, platinum, chromium, tantalum, and copper. The manufacturing process chain starts with a cleaning step with acetone and isopropanol of the stainless-steel wafer. After the deposition of the insulation layer out of Al_2O_3 according to Section III-A1, photolithography is used for the structuring of the thin-film sensor layers. Therefore, the photoresist AZ 5214 was spin-coated with a thickness of 4.3 µm at 500 r/min. A soft bake at 105 °C for 100 s was used to stabilize the photoresist. Afterward, the illumination took place within the mask aligner MA6 from SUESS with a mercury vapor lamp at 250 W for 15 s. For structuring, a foil mask was used that produces quarter-bridge sensors according to Fig. 3 (left). It consists of a meander shape pattern with ten lines next to each other with a width of 100 µm and a length of 3500 µm, whereas the two outer lines have a length of 4000 µm. They are connected through nine meander curves, resulting in a total length of 38.7 mm.

After the illumination, the development takes place in AZ 351B for 60 s (one part AZ 351B and four parts water). Now, the deposition of the different sensor layers takes place according to Table IV. The base pressure was below 1×10^{-5} mbar, and the sputtering pressure was between 6×10^{-3} and 7.0×10^{-3} mbar. Prior to deposition, a sputter etching process at 250 W with an Ar flow of 50 sccm for

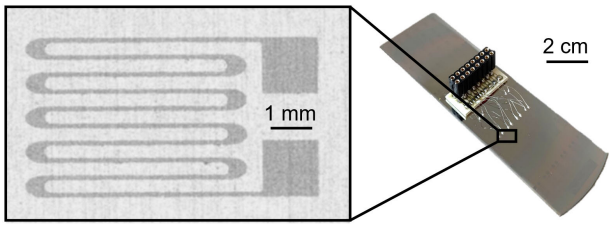

Fig. 3. (Left) Sensor design for evaluation of the k-factor and the TCR. (Right) Tensile test specimens with thin-film strain gauges.

TABLE IV
PARAMETERS FOR SPUTTERING OF SEVERAL METAL SENSOR LAYERS. THE ARGON FLOW WAS CONSTANT AT 50 sccm FOR ALL MATERIALS

Material	Magnetron	Power (W)	Sputter rate (nm/min)	Thickness (nm)	Resistivity (10^{-4} Ωcm)
Au	no	200	20.0	430	0.054 ± 0.00052
Constantan	no	200	11.7	220	1.833 ± 0.207
Cu	yes	100	14.7	230	0.035 ± 0.00043
Cr	yes	200	19.1	600	0.546 ± 0.015
NiCr5050	yes	200	50.4	430	1.709 ± 0.147
NiCr6040	no	250	13.3	300	1.236 ± 0.033
NiCr8020	yes	500	63.0	500	0.887 ± 0.078
Ta	yes	200	17.6	210	1.856 ± 0.041
Ti	yes	250	15.7	200	1.955 ± 0.098
Pt	no	200	12.0	180	0.350 ± 0.002

5 min cleans and activates the surface to increase the sensor layer adhesion. After deposition, a liftoff process in acetone with ultrasonic support removes the photoresist. Afterward, the wafers were cut with a guillotine shear to receive 30-mm-wide tensile specimens for the characterization concerning the sensor's strain sensitivity. The contacting was done with conductive two-component silver epoxy adhesive, thin wires, and a circuit board with a female connector strip that enabled the connection to a QuantumX MX1615B universal measuring amplifier module from Hottinger Baldwin Messtechnik GmbH.

2) Characterization of the Sensor Layer: First, the layer thicknesses and electrical resistances were measured to determine the resistivity. The results are summarized in Table IV. Afterward, the characterization took place regarding the two most important properties of strain gauges, which are the strain sensitivity (k-factor k) and the temperature sensitivity (TCR). They show the resistance change ΔR in contrast to the initial resistance R_0 due to a change in strain $\Delta\varepsilon$ or a change in temperature ΔT, as shown in (3) and (4).

The characterization of the k-factor was done with a tensile test stand type MultiText 2.5-xt from Mecmesin with cyclic loads between 400 and 2400 N. The elongation was calculated based on the cross-sectional area A of 24 mm^2 and Young's modulus E of 200 000 N/mm^2 (stainless-steel 1.4301) leading to strain values of 83 and 500 μm/m according to (5) that are used for the calculation of $\Delta\varepsilon$. Afterward, a hot plate was used for the determination of the TCR with temperature cycles between 30 °C and 100 °C. For both methods, the resistance values were recorded continuously to ensure linear strain or temperature behavior

$$k = (\Delta R/R_0)/\Delta\varepsilon \tag{3}$$

$$\mathrm{TCR} = (\Delta R/R_0)/\Delta T \tag{4}$$

$$\varepsilon = F/(E \cdot A). \tag{5}$$

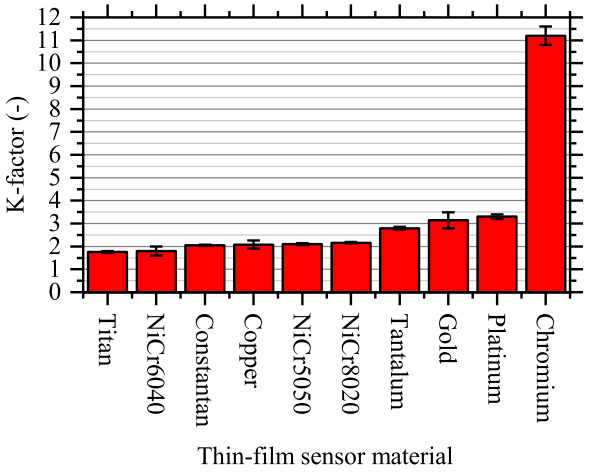

Fig. 4. K-factors for different metallic thin-film sensor materials.

The results for all investigated sensor materials are shown in Fig. 4. As expected, the Constantan layer and the NiCr alloys showed k-factors of around 2. For constantan thin films, the literature shows the highest values of 2.2 [64]. For NiCr5050, García-Alonso et al. [65] achieved a value of 2.3. Higher k-factors were reached for Au and Pt. No literature values for pure chromium thin films were found. Here, the processed strain gauges revealed the highest k-factor of 11.2 ± 0.4. This results in a sensitivity increase of at least a factor of 5 compared to conventional strain gauge materials such as Constantan or NiCr alloys. Since the measured k-factor is higher than expected, the tests were repeated with the sputtering system type MRC from Kenotec. Here, a k-factor of 11.3 ± 0.5 resulted that confirmed the measurements. Literature values could be found for Cr–O films with elevated k-factors between 4.7 (39 at% O_2) and 10.3 (7 at% O_2) due to semiconductor properties [33]. For Cr–N films, values of 8–16 [30] are reported. Therefore, it is most likely that the high k-factor of chromium is due to an oxygen or nitrogen content in the film. EDS measurements on silicon substrates showed values of up to 6 at% oxygen, but the distinction of chromium and oxygen is difficult due to similar energy values for electron transitions. Since the resistivity of 0.55 × 10^{-4} Ω·cm in Table IV is comparable to the literature range for chromium (from 0.58 × 10^{-4} to 1.07 × 10^{-4} Ω·cm [66]), it is assumed that the oxygen content is significantly lower. No nitrogen could be found according to EDS. Impurities with oxygen or nitrogen might be due to the argon 5.0 sputtering gas that contains up to 2-ppm oxygen and up to 5-ppm nitrogen [67]. Raman spectrometer measurements of chromium with a thickness of 500 nm sputtered on borosilicate glass confirmed the presence of Cr_2O_3 with peaks at 304, 347, and 547 cm^{-1}, which is in agreement with the literature [68]. No significant peaks for CrN could be detected compared to literature values [69]. Nevertheless, the amount of oxygen could not be measured. However, due to the fact that the resistivity is not increased, the final reason for the increased k-factor of chromium cannot be explained with certainty. Further research has to be carried out.

To ensure temperature stability, five chromium sensors were tested after a heat treatment at 100 °C for 1 h. Only

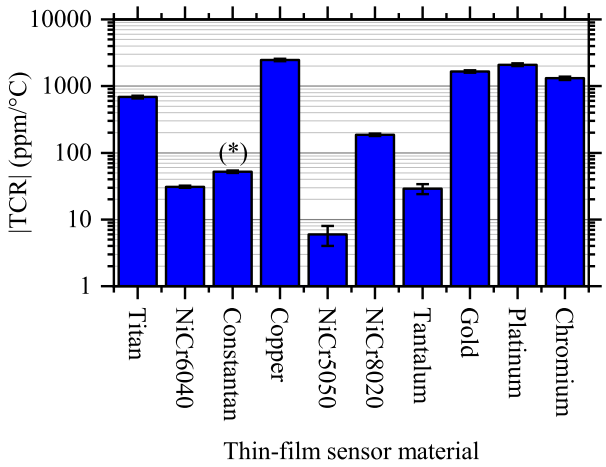

Fig. 5. Overview of the TCR values for different thin-film metallic sensor materials. (*) means a negative value.

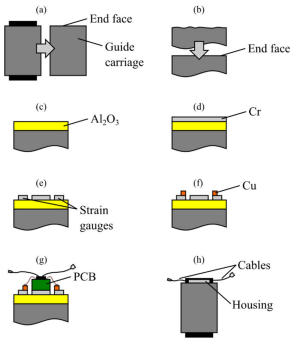

Fig. 6. Schematic process sequence for the production of sensor-integrated guide carriages. (a) Demounting. (b) Grinding, polishing, and cleaning. (c) Sputtering of the insulation layer. (d) Sputtering of the sensor layer. (e) Laser structuring. (f) Sputtering of the contact pads. (g) Contacting. (h) Mounting.

slight changes could be measured concerning the k-factor (11.4 ± 0.3), which is within the standard deviation. Optical investigations did not show any cracking that is sometimes observed depending on the substrate material [70]. Besides the information about the strain sensitivity, the temperature behavior is important information for signal stability and thermal noise. For all investigated sensor layer materials, the TCR values are shown in Fig. 5. In general, for Constantan and NiCr alloys, the TCR values are low compared to typical metals, which is one of the main reasons why these alloys are used for conventional foil-based strain gauges as the sensor layer. The literature shows thin-film values of 10 ppm/°C for Constantan [64] and values below 20 ppm/°C for NiCr50:50 [65], corresponding to the TCR values of Fig. 5. It is interesting to mention that the lowest TCR (6 ppm/°C) was measured for NiCr5050. Typically, the pure metal values for thin films are higher (Pt: 2600 ppm/°C [20], Au: 500–1500 ppm/°C [71], Cu: 1060–4270 ppm/°C [72], [73], and Cr: 1500–2200 ppm/°C [74]). Copper showed the highest value with 2470 ppm/°C, which corresponds to the literature. The reason for this high value might be due to the face-centered cubic crystal structure, which makes it very susceptible to temperature changes due to temperature-induced atom vibration and therefore hindered electron movement (electron scattering at phonons) [75]. This correlates with the decreasing mean free path length of the conductive electrons with increasing temperature [76]. For Cr, the measured TCR value of 1310 ± 80 ppm/°C is comparable with the literature and leads to the conclusion that the previously mentioned oxygen content in the film is low.

In summary, the material investigation of ten thin-film strain gauge materials showed the most promising results with chromium. With a k-factor of 11.2, a material was found that has the potential to enable force measurements at the guide carriage with a low response threshold and high SNR so that extremely low strain values could be resolved.

IV. Sensory Guide Carriage

A. Manufacturing

To enable the deposition on the guide carriage, some adaptations of the sputter system were necessary. The position of the target materials was elevated with cylindric extension cylinders, and the heating station in the substrate plate was removed so that the remaining distance between the target surface and the surface of the guide carriage resulted to approximately 61 mm compared to the 88 mm present in the case of conventional wafer deposition. In addition, a stainless-steel foil was installed underneath the target to build a cylindrical dark room shielding. The complete manufacturing is shown in the schematic drawings in Fig. 6.

Prior to deposition, the guide carriage was demounted. The rollers and the complete roller return system were removed, and the remaining guide carriage was chemically cleaned with acetone and isopropanol to remove the remaining grease. Then, for the deposition of a functioning insulation layer, the grinding and polishing machine QATM QPol 250 A2-ECO was used to reduce the mean roughness R_a and the mean roughness depth R_z of one end face from 320 ± 70 nm and 2330 ± 420 nm to 29 ± 4 nm and 265 ± 65 nm. Again, these values were measured with the tactile roughness tester. Now, with a power of 200 W and an Ar gas flow of 50 sccm, a sputter etching step was done. For the Al_2O_3 deposition, the power had to be adapted from 400 W (Section III-A1) to 300 W, which was necessary most likely due to increased temperature development because of decreased heat transfer to the cooled substrate plate caused by the guide carriage geometry. To reduce stochastically occurring defects (impurities and pin holes), the insulation layer deposition took place in five steps of 900 nm each. This procedure was adapted from [58]. The layer height was measured on a reference Si chip with a tactile profilometer (Dektak XT from Bruker). In addition, the Ar flow was changed to 90 sccm. The O_2 flow was kept constant at 3 sccm without using the restrictor setting of the high vacuum pump. The bias voltage was in the range between 100 and 700 V. The result was a sputter pressure of 7.2×10^{-3} mbar, no target poisoning, and a stoichiometry of Al:O = 40:60 that was confirmed by EDS measurements. The result can be seen in Fig. 7(a).

To achieve suitable resistance values of the single strain gauges of the aimed thin-film full bridges in the range between 120 and 1000 Ω, a chromium layer with a thickness of 100 nm was sputter coated [Fig. 7(b)]. These resistance values are limits of the strain gauge amplifier that should be used later.

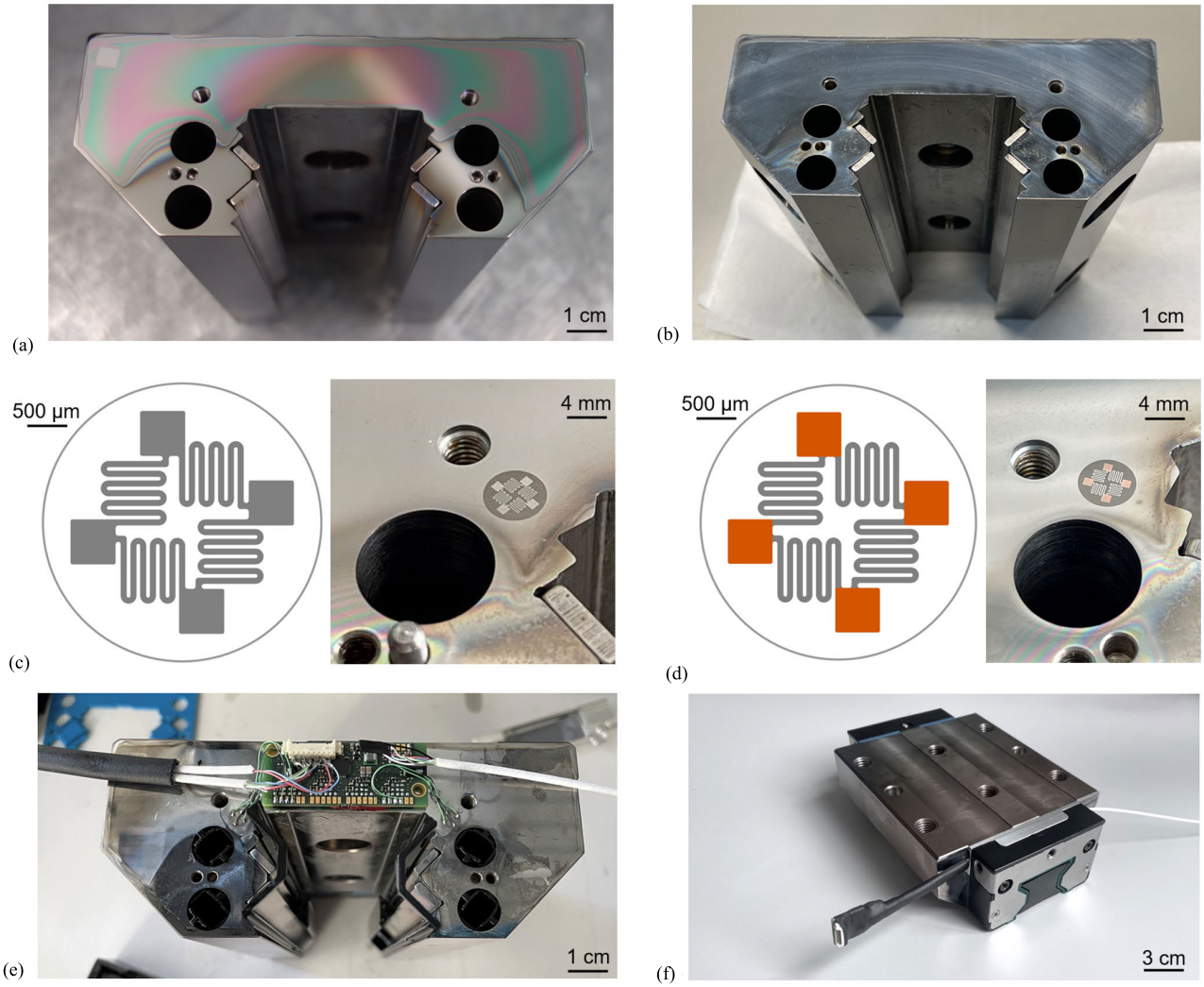

Fig. 7. (a) Deposition of the Al_2O_3 insulation layer. (b) Deposition of the Cr sensor layer. (c) Laser structuring of the sensor layer. (d) Structured deposition of the Cu contact pads using shadow masks. (e) Integration of the strain gauge amplifier PCB board. (f) Thin-film sensor integrated guide carriage with cables for setting, supply, and reading of the PCB board.

TABLE V
LASER PARAMETERS FOR STRUCTURING A 100-nm CHROMIUM THIN FILM

Parameter	Value
Power / Optical power	25 % / 100 mW
Velocity / Frequency	800 mm/s / 160 kHz
Pulse duration (FWHM) / Repetitions	55 ns / 5
Laser point variable / Filling interval	0 / 5 µm

Since conventional photolithography is not possible for the guide carriage, a laser ablation process is used for structuring [77], [78]. Therefore, a UV solid-state laser (Nd:YVO4) MD-U1000C from Keyence ($\lambda = 355$ nm) structured the thin film with the parameters in Table V.

The sensor layout in Fig. 7(c) consists of a full-bridge inside of a 5 mm diameter. Each strain gauge has seven lines with a width of 100 μm and a length of 900 μm. Their position and alignment are implemented according to the simulation results presented in Section II.

After the laser ablation process shown in Fig. 7(c), the contact pads were sputter-coated with copper through a 100-μm-thick laser-cut steel shadow mask [Fig. 7(d)]. For optimal contact with the guide carriage, it was fixed with an aluminum sheet that has the corresponding holes in the area of the contact pads. Dowl pins ensured the alignment (± 20 μm) connecting the guide carriage with the shadow mask and the aluminum sheet. Investigations showed sufficient soldering for a thickness of 600 nm. Now, the contacting was done by soldering with Sn60Pb39Cu1 on the contact pads. In contrast to previous contacting methods with conductive adhesive [8], [10], [59], the solder connection offers lower contact resistance (10 mΩ instead of 1–5 Ω) and minimizes measurement noise. The wires lead to a strain gauge amplifier type XN5 from Texense. It enables the connection to both full bridges at the same time in Fig. 7(e). Two cables lead out of the guide carriage: one of them for the energy supply and the strain gauge full-bridge voltages and the other one for the USB connection for a user interface to change the amplifier settings. The integration of the sensors and the amplifier

board was enabled through the adaptation of one roller guide. Material was removed to generate space for an aluminum housing. Now, the rollers and the complete roller return system were mounted. Finally, a sensor-integrated guide carriage with directly deposited thin-film sensors resulted, which is shown in Fig. 7(f).

B. Sensor Characterization

Before the sensor signals are evaluated with static loads, the electrical thin-film values were measured. Values of 350 GΩ were measured with the Ohm and Current Meter TO3 from Fischer Elektronik for the insulation layer with a total thickness of approximately 4.5 μm, resulting in a resistivity of 4.5×10^{13} Ω·cm. Even though these values are up to factor 10 lower compared to the initial results on the wafer level from Section III-A2, they are sufficient for reliable use of the strain gauges. Reasons might be the necessary change of the geometrical sputtering conditions and the different roughness values of the metallic surface.

Since the sensor design shown in Fig. 7(d) already connects the four single strain gauges to one full bridge, it is not possible to measure the single resistance values of the four strain gauges R_1–R_4 anymore. Nevertheless, the parallel connection of one strain gauge with the corresponding remaining three strain gauges can be measured. These four possible measurement arrangements lead to a linear system of four equations, which is solved iteratively due to measurement uncertainties according to (6) (exemplary for strain gauge R_1 parallel to R_2–R_4)

$$R_1||R_{2,3,4} = R_1 \cdot (R_2 + R_3 + R_4)/(R_1 + (R_2 + R_3 + R_4)). \tag{6}$$

The results are shown in Table VI. Here, the measured and calculated values are shown. Accumulated measurement errors resulting from the iterative calculation are in the range of 1×10^{-5} Ω and are therefore negligible. The measured bridge offsets show sufficient values below 15 mV/V. The comparison with the calculated bridge values based on the calculated resistance values proves the overall process since only small deviations occur.

Now, the strain gauge amplifier was provided with a supply voltage of 12 V by a voltage source (see Fig. 8). With two strain gauge full bridges connected, a current of 20 ± 1 mA resulted. The amplifier itself generates a supply voltage of 5 V for the full bridges. The bridge voltage values were recorded with a strain gauge measurement amplifier-type QuantumX MX1615B (see Fig. 8).

To use the most suitable strain gauge amplifier settings, both full-bridge offset values were initially corrected as much as possible according to the measured bridge offset values. Then, the gain factor was set to the maximum value of 1000 for maximum signal due to the expected low strain. Finally, the remaining output signals of the strain gauge amplifier were shifted to an output value of 2.5 V to guarantee a similar measurement range in both strain directions (elongation and compression) since the output is between 0 and 5 V.

TABLE VI
SINGLE STRAIN GAUGE RESISTANCE AND BRIDGE OFFSET VALUES

Full-bridge	Parallel Connection (-)	Measurement value (Ω)	Strain Gauge (-)	Calculated Value (Ω)
S1 (left)	$R_1 \parallel R_{2,3,4}$	180.1	R_1	242.9
	$R_2 \parallel R_{3,4,1}$	170.8	R_2	225.0
	$R_3 \parallel R_{4,1,2}$	174.7	R_3	232.8
	$R_4 \parallel R_{1,2,3}$	177.2	R_4	236.8
	Mean value	175.7 ± 3.4	Mean value	234.3 ± 6.8
	Bridge offset	12.8 mV/V	Bridge offset	14.9 mV/V
S2 (right)	$R_1 \parallel R_{2,3,4}$	325.4	R_1	431.7
	$R_2 \parallel R_{3,4,1}$	357.3	R_2	499.8
	$R_3 \parallel R_{4,1,2}$	324.8	R_3	430.6
	$R_4 \parallel R_{1,2,3}$	303.7	R_4	390.8
	Mean value	327.8 ± 19.1	Mean value	438.2 ± 39.2
	Bridge offset	11.3 mV/V	Bridge offset	12.3 mV/V

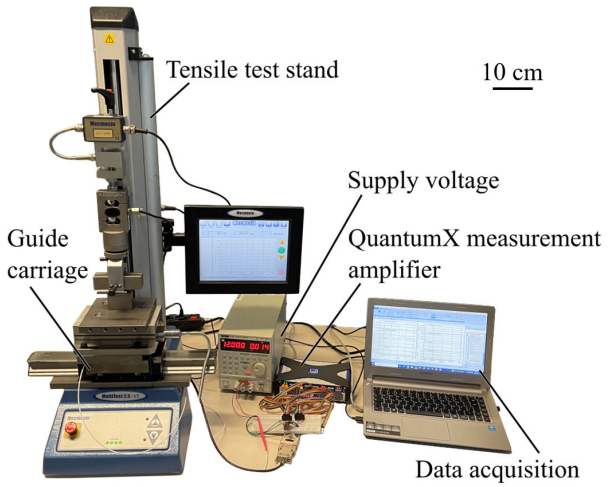

Fig. 8. Measurement setup: guide carriage in a tensile test stand.

Then, the guide carriage was integrated into a tensile test stand-type MultiText 2.5-xt from Mecmesin (Fig. 8). Therefore, several steel adapter plates were used that enabled the fixation of a guide rail-type CS RSA-045-SNS-U-MA-SK with a length of 400 mm in two different positions so that a force introduction on the guide carriage (placed on the guide rail) was possible in the z-direction as well as in the y-direction [see Fig. 9(a) and (b)]. A clamping device allowed tensile and compressive stress. Besides the measurement of the two full bridges, the force is also recorded. The test procedure contains two cycles with forces ranging from −2400 to 2400 N so that both tensile and compression stresses are present. The results for both directions are shown in Fig. 9(c) and (d).

As expected, the sensor signals for the z-direction in Fig. 9(c) show similar behavior with deflection in the same direction with sensitivities of 1.81 ± 0.04 mV/kN (S1) and 1.18 ± 0.07 mV/kN (S2). Here, a positive load represents compression. The difference might be due to different positions of the rollers or even different numbers of rollers that are exposed to load. An influence of slight asymmetries of the complete mechanical measurement setup could also be the reason. The

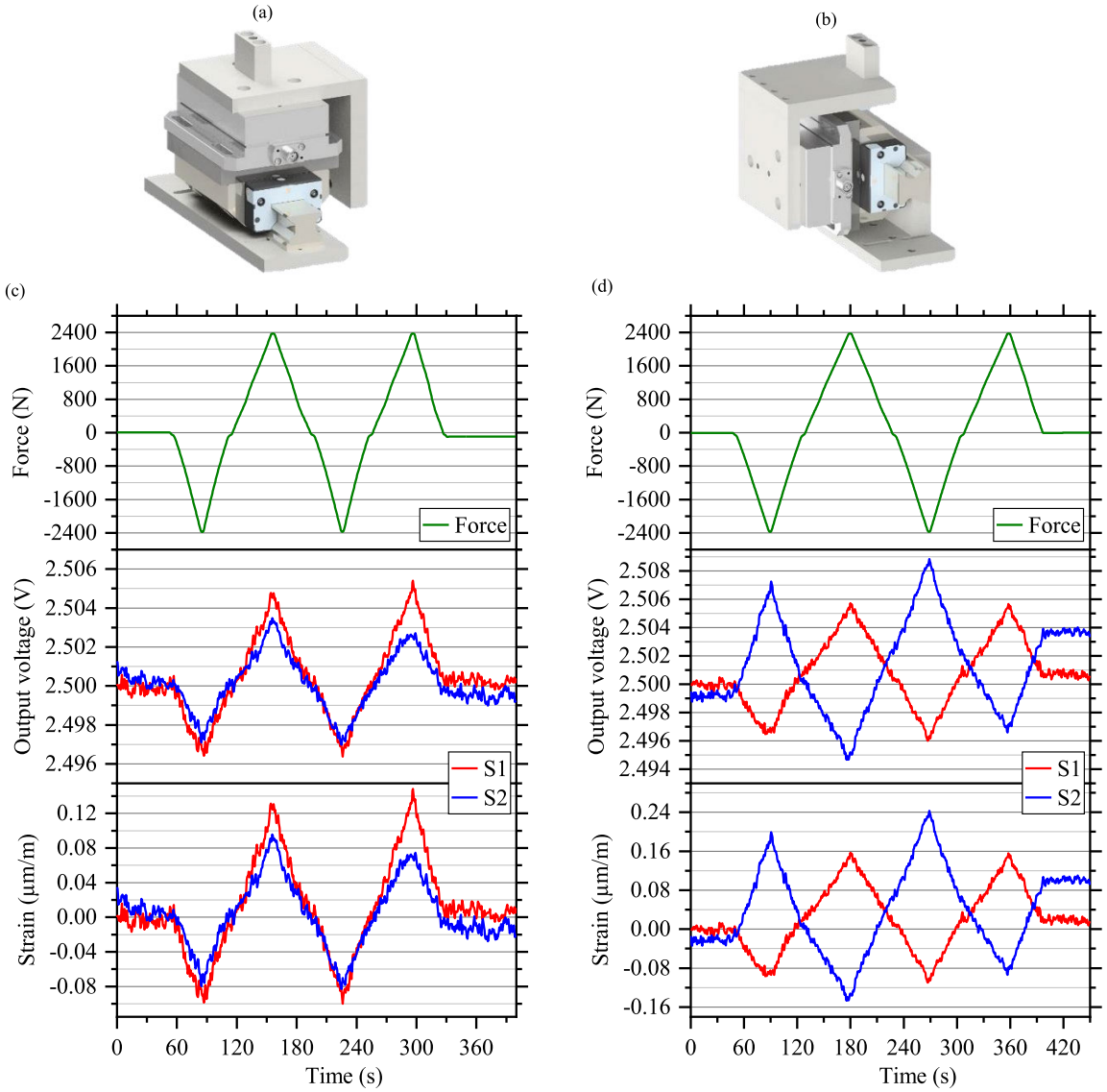

Fig. 9. Setup for force introduction in (a) z-direction and (b) y-direction. Measurement signals due to force introduction in (c) z-direction and (d) y-direction.

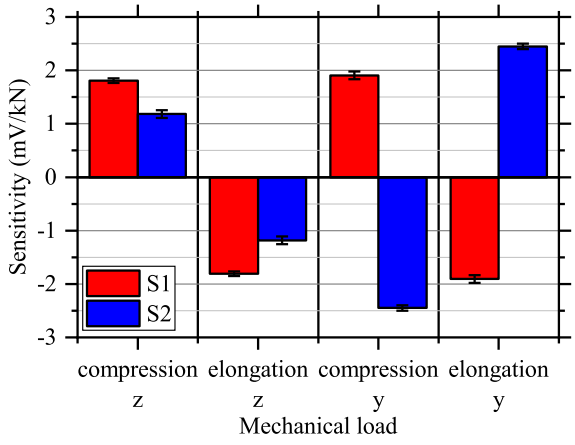

Fig. 10. Comparison of sensitivities for compression and elongation load applied in the z- and y-directions on the guide carriage. Positive values correspond to compression [compare Fig. 9(a) and (b)]. The results are in agreement with the assumptions made in Table I.

conversion to strain values according to (7) [79] with Poisson's ratio $\nu = 0.3$, the measured output bridge voltage U_O, and the supply bridge voltage $U_S = 5$ V results in 0.20 and 0.15 μm/m for the whole force range

$$\varepsilon = 4/k \cdot (1/2) \cdot 1/(1+\nu) \cdot U_O/U_S. \tag{7}$$

The simulation in Section II revealed values of ± 3 μm/m. Possible reasons for the deviation are the same as mentioned above. The noise is in the range of 0.02 μm/m (20 nm/m), which shows the high sensitivity of the developed sensors. An almost linear behavior can be seen for the elongation as well as for the compression phase.

In the y-direction, full bridge S1 has a sensitivity of 1.91 ± 0.07 mV/kN, whereas S2 shows a value of -2.45 ± 0.05 mV/kN. The force here is assumed to lead to compression if it is positive. A linear behavior can be seen over the complete load range. Strain values of 0.22 and 0.34 μm/m are calculated with similar noise as it is mentioned for the z-direction. As seen in the graphs, a slight nonlinearity occurs when the compression phase turns into the elongation phase and vice versa ($F = 0$ N). This is due to the measurement setup and can be explained by the slight play that

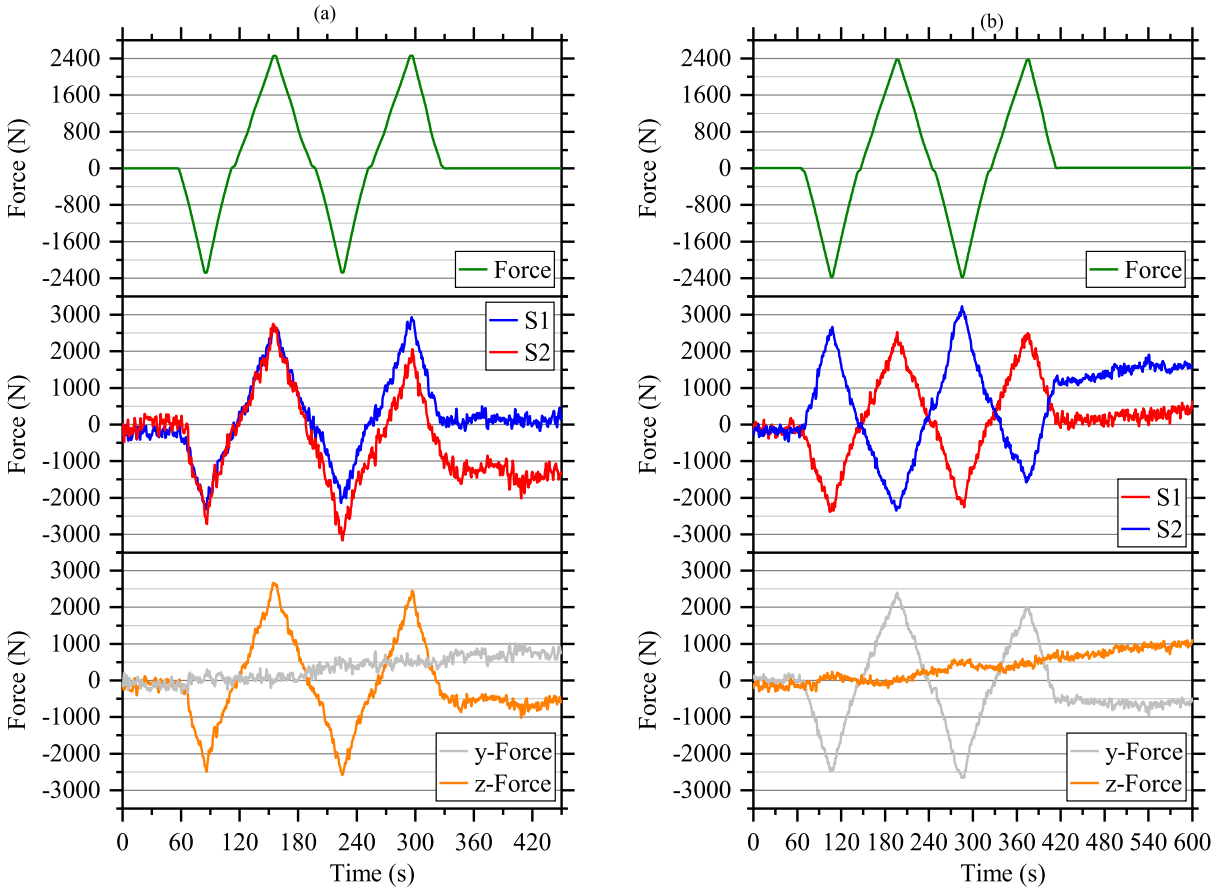

Fig. 11. Force calculation with force introduction in (a) z-direction and (b) y-direction.

the components have, especially the clamping device. Even though the measurement duration is only about 6 min, there is already a signal drift visible with maximum strain values of 0.12 μm/m.

A summary of the sensitivities can be seen in Fig. 10. As it becomes obvious, the four different mechanical load cases with compression and elongation in the z- and y-directions can be distinguished as it was assumed initially in Table I.

After this characterization, the test procedure is repeated once again to measure the actual forces with the determined sensitivities, as depicted in Fig. 11. The full-bridge signals are illustrated in red (S1) and blue (S2) and should follow the force signal of the tensile test stand in green once again based on (8) and (9). Here, the sensitivities a_{S1} and a_{S2} are used

$$F_{S1} = (U_{O\_S1} - 2.5\ V)/a_{S1} \tag{8}$$

$$F_{S2} = (U_{O\_S2} - 2.5\ V)/a_{S2}. \tag{9}$$

The addition and subtraction based on (10) and (11) result in a statement about the final force values for the z- and y-directions

$$F_z = (F_{S1} + F_{S2})/2 \tag{10}$$

$$F_y = (F_{S1} - F_{S2})/2. \tag{11}$$

It becomes clear that the direction of the force introduction can be predicted. For the forces that should be zero during the tests [gray line in Fig. 11(a) and orange line in Fig. 11(b)], no force cycles occur. Nevertheless, a drift behavior can be seen for all measurements with values between 500 N for the investigated force direction and 1 kN for the passive force direction.

V. Conclusion

This article showed the development of a sensor-integrated guide carriage based on thin-film strain gauges. Several sensor layer materials were tested concerning their k-factor and TCR. Chromium was chosen as a sensor material since it revealed the highest k-factor of 11, which was necessary according to the FEM simulation results to reach sufficient measurement resolution.

The manufacturing of the strain gauges on one end face of the guide carriage included a grinding and polishing step, coating of an Al_2O_3 insulation layer, the chromium sensor layer, laser structuring, and coating of the copper contact pads for soldering. A circuit board was completely integrated without changing the guide carriage dimensions and amplified the strain gauge full-bridge signals so that output voltages between 0 and 5 V resulted. In a tensile test stand, the sensor-integrated guide carriage was placed on a guide rail. Here, with only two sensors and their sensor data fusion, the measurement of tensile and compressive forces in the z-direction and y-direction was enabled. The result was a mean

sensitivity of 1.49 mV/kN in the z-direction and 2.18 mV/kN in the y-direction. The test forces of maximum $\pm$2400 N led to strain values in the range of 0.15–0.4 μm/m at the two sensor positions. In comparison, the simulation showed values of around $\pm$3 μm/m for 1 kN.

Further development steps should address a method for laser trimming of the initial single strain gauge resistance values of the full bridges to achieve even lower bridge offset values. It is assumed that this would have a positive impact on the strain and drift behavior that has to be investigated.

With the knowledge developed in this article for static strain measurements on guide carriages, the measurement can now be extended to dynamic load measurements when a single guide carriage is moving on a guide rail. Afterward, the sensor-integrated guide carriages will be used in combination to replicate a realistic scenario as it is present in machine tools such as in portal milling machines. With intelligent sensor data fusion, force information about the whole guide system should be derived.

REFERENCES

[1] E. Kirchner et al., "A review on sensor-integrating machine elements," *Adv. Sensor Res.*, vol. 3, no. 4, Apr. 2024, Art. no. 2300113, doi: 10.1002/adsr.202300113.

[2] *Compact Gantry Milling Machine Endura® 7000Linear*, Fooke GmbH, Borken, Germany, 2022. [Online]. Available: https://www.fooke-machines.com/en/milling-machines/compact-gantry-milling-machine-endura-7000linea

[3] *Roller Carriage RWD-055-FNS-C2-P-2*, Bosch Rexroth, Schweinfurt, Germany, Accessed: Feb. 5, 2022. [Online]. Available: https://store.boschrexroth.com/Linear-Motion-Technology/Linear-guides/Roller-rail-systems/ROLLER-RUNNER-BLOCK-CARBON-STEEL_R18515222X?cclcl=en_US

[4] B. Denkena, B. Bergmann, P. Schreiber, A. Schmidt, and M. Klaproth, "Sensing linear roller guide carriages for condition monitoring applications," in *Proc. 21st Machining Innov. Conf. Aerosp. Ind.*, Hannover, Germany, 2021, pp. 78–81, doi: 10.2139/ssrn.3936526.

[5] B. Denkena, J.-K. Park, B. Bergmann, and P. Schreiber, "Force sensing linear rolling guides," in *Proc. Euspen's 18th Int. Conf. Exhib.*, Venice, Italy, 2018, pp. 1–2. [Online]. Available: https://www.euspen.eu/knowledge-base/ICE18269.pdf

[6] B. Denkena et al., "Force sensing linear rolling guides based on modified metal strain gauges," in *Proc. Euspen's 23rd Int. Conf. Exhib.*, Copenhagen, Denmark, 2023, pp. 1–2. [Online]. Available: https://www.euspen.eu/knowledge-base/ICE23258.pdf

[7] D. Klaas, J. Becker, M. C. Wurz, J. Schlosser, and M. Kunze, "New coating system for direct-deposition of sensors on components of arbitrary size," in *Proc. IEEE Sensors*, Orlando, FL, USA, 2016, pp. 1–3, doi: 10.1109/ICSENS.2016.7808440.

[8] D. Klaas, R. Ottermann, F. Dencker, and M. C. Wurz, "Development, characterisation and high-temperature suitability of thin-film strain gauges directly deposited with a new sputter coating system," *Sensors*, vol. 20, no. 11, p. 3294, Jun. 2020, doi: 10.3390/s20113294.

[9] R. Ottermann, N. Kyoushi, and M. C. Wurz, "Direct-deposited thin-film strain gauges for high-temperature applications," in *Proc. MikroSystemTechnik Kongress*, Dresden, Germany, 2023, pp. 1–4. [Online]. Available: https://www.vde-verlag.de/proceedings-de/456203168.html

[10] R. Ottermann et al., "Direct deposition of thin-film strain gauges with a new coating system for elevated temperatures," in *Proc. IEEE Sensors*, Rotterdam, The Netherlands, 2020, pp. 1–4, doi: 10.1109/SENSORS47125.2020.9278661.

[11] R. Ottermann et al., "Directly deposited thin-film strain gauges on curved metallic surfaces," in *Proc. IEEE Sensors*, Sydney, NSW, Australia, 2021, pp. 1–4, doi: 10.1109/SENSORS47087.2021.9639542.

[12] D. Klaas, "Technology development for direct-deposition and structuring of sensor systems on especially large components by the example of strain gauges—Technologieentwicklung zur Direktabscheidung und Strukturierung von Sensorik auf insbesondere Großbauteilen am Beispiel von Dehnungsmessstreifen," Doctor Thesis, Inst. Micro Prod. Technol., Leibniz Univ. Hannover, Hanover, Germany, 2021.

[13] D. Konopka et al., "Advancements in monitoring of tribological stress in bearings using thin-film strain gauges," in *Proc. Eccomas*, Patras, Greece, 2023, pp. 1–12, doi: 10.7712/150123.9934.443603.

[14] S. Keil, *Dehnungsmessstreifen—Strain Gauges*, 2nd ed., Wiesbaden, Germany: Springer, 2017. [Online]. Available: https://link.springer.com/book/10.1007/978-3-658-13612-3

[15] H. Chiriac, M. Urse, F. Rusu, C. Hison, and M. Neagu, "Ni–Ag thin films as strain-sensitive materials for piezoresistive sensors," *Sens. Actuators A, Phys.*, vol. 76, nos. 1–3, pp. 376–380, Aug. 1999, doi: 10.1016/S0924-4247(99)00027-8.

[16] U. Heckmann, R. Bandorf, H. Gerdes, M. Lübke, S. Schnabel, and G. Bräuer, "New materials for sputtered strain gauges," *Proc. Chem.*, vol. 1, no. 1, pp. 64–67, Sep. 2009, doi: 10.1016/j.proche.2009.07.016.

[17] H. Gerdes, R. Bandorf, U. Heckmann, V. Schmidt, H. Kricheldorf, and G. Bräuer, "Sputter deposition of strain gauges using ITO/Ag," *Plasma Processes Polym.*, vol. 6, no. S1, pp. 813–816, Jun. 2009, doi: 10.1002/ppap.200932101.

[18] O. J. Gregory and Q. Luo, "A self-compensated ceramic strain gage for use at elevated temperatures," *Sens. Actuators A, Phys.*, vol. 88, no. 3, pp. 234–240, Jan. 2001, doi: 10.1016/S0924-4247(00)00513-6.

[19] P. Schmid et al., "Impact of adhesion promoters and sputter parameters on the electro-mechanical properties of Pt thin films at high temperatures," *Sens. Actuators A, Phys.*, vol. 285, pp. 149–157, Jan. 2019, doi: 10.1016/j.sna.2018.11.010.

[20] S. Fricke, A. Friedberger, G. Müller, H. Seidel, and U. Schmid, "Strain gauge factor and TCR of sputter deposited Pt thin films up to 850 °C," in *Proc. IEEE Sensors*, 2008, pp. 1532–1535, doi: 10.1109/ICSENS.2008.4716739.

[21] A. Shokuhfar, P. Heydari, M. R. Aliahmadi, M. Mohtashamifar, S. Ebrahimi-Nejad R., and M. Zahedinejad, "Low-cost polymeric microcantilever sensor with titanium as piezoresistive material," *Microelectronic Eng.*, vol. 98, pp. 338–342, Oct. 2012, doi: 10.1016/j.mee.2012.07.067.

[22] M. R. Neuman and W. G. Sutton, "Structural dependence of strain gauge effect and surface resistivity for thin gold films," *J. Vac. Sci. Technol.*, vol. 6, no. 4, pp. 710–713, Jul. 1969, doi: 10.1116/1.1315737.

[23] H. M. Kalpana and V. S. Prasad, "Development of the invar36 thin film strain gauge sensor for strain measurement," *Meas. Sci. Technol.*, vol. 25, no. 6, Jun. 2014, Art. no. 065102, doi: 10.1088/0957-0233/25/6/065102.

[24] C. Zarfl, P. Schmid, G. Balogh, and U. Schmid, "Electro-mechanical properties and oxidation behaviour of $TiAlN_xOy$ thin films at high temperatures," *Sens. Actuators A, Phys.*, vol. 226, pp. 143–148, May 2015, doi: 10.1016/j.sna.2015.02.026.

[25] P. Schmid et al., "Influence of the AlN/Pt-ratio on the electro-mechanical properties of multilayered AlN/Pt thin film strain gauges at high temperatures," *Sens. Actuators A, Phys.*, vol. 302, Feb. 2020, Art. no. 111805, doi: 10.1016/j.sna.2019.111805.

[26] G.-S. Chung, "Characteristics of tantalum nitride thin film strain gauges for harsh environments," *Sens. Actuators A, Phys.*, vol. 135, no. 2, pp. 355–359, Apr. 2007, doi: 10.1016/j.sna.2006.07.025.

[27] I. Ayerdi, E. Casta no, A. Garcia-Alonso, and F. J. Gracia, "Ceramic pressure sensor based on tantalum thin film," *Sens. Actuators A, Phys.*, vol. 42, nos. 1–3, pp. 435–438, Apr. 1994, doi: 10.1016/0924-4247(94)80028-6.

[28] O. J. Gregory, A. B. Slot, P. S. Amons, and E. E. Crisman, "High temperature strain gages based on reactively sputtered AlNx thin films," *Surf. Coatings Technol.*, vol. 88, nos. 1–3, pp. 79–89, Jan. 1997, doi: 10.1016/S0257-8972(96)02889-7.

[29] N. Dam Madsen et al., "Titanium nitride as a strain gauge material," *J. Microelectromech. Syst.*, vol. 25, no. 4, pp. 683–690, Aug. 2016, doi: 10.1109/JMEMS.2016.2577888.

[30] E. Niwa, Y. Sasaki, M. Homma, and K. Masumoto, "Cr-N strain sensitive thin films and their pressure sensor applications," in *Proc. Tech. Meeting Phys. Sensors*, vol. 134, no. 12, Jun. 2014, pp. 29–34, doi: 10.1541/ieejsmas.134.132.

[31] E. Niwa and H. Mikami, "Strain sensors and pressure sensors using Cr-N thin films for high pressure hydrogen gas," *IEEJ Trans. Sensors Micromachines*, vol. 138, no. 5, pp. 178–184, 2018, doi: 10.1541/ieejsmas.138.178.

[32] E. Niwa et al., "Load vector sensors using strain-sensitive Cr-N thin films and their applications," *Electron. Commun. Jpn.*, vol. 99, no. 4, pp. 58–67, Apr. 2016, doi: 10.1002/ecj.11803.

[33] H. Yamadera and Y. Taga, "Cr-O-X film as a strain gauge," *Thin Solid Films*, vol. 206, nos. 1–2, pp. 107–110, Dec. 1991, doi: 10.1016/0040-6090(91)90401-I.

[34] H. Schmid-Engel, S. Uhlig, U. Werner, and G. Schultes, "Strain sensitive Pt-SiO_2 nano-cermet thin films for high temperature pressure and force sensors," *Sensors Actuators A, Phys.*, vol. 206, pp. 17–21, Feb. 2014, doi: 10.1016/j.sna.2013.11.021.

[35] P. J. French and A. G. R. Evans, "Polycrystalline silicon as a strain gauge material," *J. Phys. E, Sci. Instrum.*, vol. 19, no. 12, pp. 1055–1058, Dec. 1986, doi: 10.1088/0022-3735/19/12/016.

[36] H. Schaumburg, *Sensoren—Sensors*, 1st ed., Wiesbaden, Germany: Vieweg+Teubner Verlag, 1992, doi: 10.1007/978-3-322-99927-6.

[37] D. Krampert, S. Unsleber, and L. Reindl, "Localized surface strain measurement for load detection using diamond like carbon coating on a linear guide," in *Proc. IEEE Int. Instrum. Meas. Technol. Conf. (IMTC)*, May 2021, pp. 1–6, doi: 10.1109/I2MTC50364.2021.9459827.

[38] D. Krampert, S. Unsleber, C. Janssen, and L. Reindl, "Load measurement in linear guides for machine tools," *Sensors*, vol. 19, no. 15, p. 3411, Aug. 2019, doi: 10.3390/s19153411.

[39] D. Krampert, S. Unsleber, and L. Reindl, "Measuring load on linear guides in different load scenarios using an integrated DLC based sensor system," in *Proc. SMSI Conf.*, 2020, pp. 73–74, doi: 10.5162/SMSI2020/A4.4.

[40] D. Krampert, M. Ziegler, S. Unsleber, L. Reindl, and S. J. Rupitsch, "On the stiffness hysteresis of profiled rail guides," *Tribology Int.*, vol. 160, Aug. 2021, Art. no. 107019, doi: 10.1016/j.triboint.2021.107019.

[41] H. Lüthje et al., "Preparation and characterization of multifunctional thin film sensors based on amorphous diamond-like-carbon," in *13th Int. Conf. Solid-State Sensors, Actuators Microsyst., Dig. Tech. Papers (TRANSDUCERS)*, 2005, pp. 2111–2114, doi: 10.1109/SENSOR.2005.1497520.

[42] S. Biehl, H. Lüthje, R. Bandorf, and J.-H. Sick, "Multifunctional thin film sensors based on amorphous diamond-like carbon for use in tribological applications," *Thin Solid Films*, vol. 515, no. 3, pp. 1171–1175, Nov. 2006, doi: 10.1016/j.tsf.2006.07.143.

[43] C. S. Smith, "Piezoresistance effect in germanium and silicon," *Phys. Rev.*, vol. 94, no. 1, pp. 42–49, Apr. 1954, doi: 10.1103/PhysRev.94.42.

[44] Y. Kanda, "Piezoresistance effect of silicon," *Sens. Actuators A, Phys.*, vol. 28, no. 2, pp. 83–91, Jul. 1991, doi: 10.1016/0924-4247(91)85017-I.

[45] S. Middelhoek et al., "Silicon sensors," *Meas. Sci. Technol.*, vol. 6, no. 12, pp. 1641–1658, Dec. 1995, doi: 10.1088/0957-0233/6/12/001.

[46] Y. Kim, Y. Kim, C. Lee, and S. Kwon, "Thin polysilicon gauge for strain measurement of structural elements," *IEEE Sensors J.*, vol. 10, no. 8, pp. 1320–1327, Aug. 2010, doi: 10.1109/JSEN.2009.2039565.

[47] Y. Kim and S. Kwon, "Resistivity dependence of gauge factor of polysilicon strain gauge," *Micro Nano Lett.*, vol. 5, no. 3, pp. 189–192, 2010, doi: 10.1049/mnl.2010.0031.

[48] H. S. Choi, Y. G. Lee, M. B. Hong, and Y. J. Choi, "A novel geometric design method of elastic structure for 6-axis force/torque sensor," *IEEE Access*, vol. 7, pp. 166564–166577, 2019, doi: 10.1109/ACCESS.2019.2953961.

[49] G. A. Kebede, A. R. Ahmad, S.-C. Lee, and C.-Y. Lin, "Decoupled six-axis force–moment sensor with a novel strain gauge arrangement and error reduction techniques," *Sensors*, vol. 19, no. 13, p. 3012, Jul. 2019, doi: 10.3390/s19133012.

[50] H. Akbari and A. Kazerooni, "Improving the coupling errors of a maltese cross-beams type six-axis force/moment sensor using numerical shape-optimization technique," *Measurement*, vol. 126, pp. 342–355, Oct. 2018, doi: 10.1016/j.measurement.2018.05.074.

[51] J.-K. Min and J.-B. Song, "Sensor block type joint torque sensor insensitive to crosstalk error," *IEEE Sensors J.*, vol. 20, no. 7, pp. 3469–3475, Apr. 2020, doi: 10.1109/JSEN.2019.2959842.

[52] Y.-J. Wang, C.-W. Hsu, and C.-Y. Sue, "Design and calibration of a dual-frame force and torque sensor," *IEEE Sensors J.*, vol. 20, no. 20, pp. 12134–12145, Oct. 2020, doi: 10.1109/JSEN.2020.2999156.

[53] Y. Wang, L. Wu, J. Ke, and T. Lu, "Planar six-axis force and torque sensors," *IEEE Sensors J.*, vol. 21, no. 23, pp. 26631–26641, Dec. 2021, doi: 10.1109/JSEN.2021.3122174.

[54] R. Shu, Z. Chu, and H. Shu, "A lever-type method of strain exposure for disk F-shaped torque sensor design," *Sensors*, vol. 20, no. 2, p. 541, Jan. 2020, doi: 10.3390/s20020541.

[55] H. Boujnah, "Kraftsensitiver Spindelschlitten zur online Detektion und Kompensation der Werkzeugabdrängung in der Fräsbearbeitung," Doctor thesis, Inst. Prod. Eng. Mach. Tools, Leibniz Univ. Hannover, Hanover, Germany, 2019.

[56] K. Kunert, "Spannungsverteilung im halbraum bei elliptischer Flächenpressungsverteilung über einer rechteckigen Druckfläche," *Forschung auf dem Gebiete des Ingenieurwesens*, vol. 27, no. 6, pp. 165–174, Nov. 1961, doi: 10.1007/bf02561354.

[57] P. Kayser, J. C. Godefroy, and L. Leca, "High-temperature thin-film strain gauges," *Sens. Actuators A, Phys.*, vols. 37–38, pp. 328–332, Jun. 1993, doi: 10.1016/0924-4247(93)80055-L.

[58] S. Heikebrügge et al., "Residual stresses from incremental hole drilling using directly deposited thin film strain gauges," *Experim. Mech.*, vol. 62, pp. 701–713, Jan. 2022, doi: 10.1007/s11340-022-00822-0.

[59] R. Ottermann, T. Steppeler, F. Dencker, and M. C. Wurz, "Degeneration effects of thin-film sensors after critical load conditions of machine components," *Machines*, vol. 10, no. 10, p. 870, Sep. 2022, doi: 10.3390/machines10100870.

[60] D. Klaas, P. Taptimthong, L. Jogschies, and L. Rissing, "Component integrated sensors: Deposition of thin insulation layers on functional surfaces," *Proc. Technol.*, vol. 15, pp. 114–121, 2014, doi: 10.1016/j.protcy.2014.09.062.

[61] H. Bartzsch et al., "Electrical insulation properties of sputter-deposited SiO_2, Si_3N_4 and Al_2O_3 films at room temperature and 400 °C," *Phys. Status Solidi A*, vol. 206, no. 3, pp. 514–519, Mar. 2009, doi: 10.1002/pssa.200880481.

[62] M. Voigt and M. Sokolowski, "Electrical properties of thin Rf sputtered aluminum oxide films," *Mater. Sci. Eng., B*, vol. 109, nos. 1–3, pp. 99–103, 2004, doi: 10.1016/j.mseb.2003.10.056.

[63] W. H. Ha, M. H. Choo, and S. Im, "Electrical properties of Al_2O_3 film deposited at low temperatures," *J. Non-Crystalline Solids*, vol. 303, no. 1, pp. 78–82, May 2002, doi: 10.1016/s0022-3093(02)00968-7.

[64] J. Gouault, M. Hubin, G. Richon, and B. Eudeline, "3.2 the electromechanical behaviour of a full component (dielectric and Cu/Ni constantan alloy) for thin film strain gauge deposited upon steel-substrate," *Vacuum*, vol. 27, no. 4, pp. 363–365, Jun. 1977, doi: 10.1016/0042-207X(77)90024-0.

[65] A. García-Alonso, J. García, E. Castaño, I. Obieta, and F. J. Gracia, "Strain sensitivity and temperature influence on sputtered thin films for piezoresistive sensors," *Sens. Actuators A, Phys.*, vols. 37–38, pp. 784–789, Jun. 1993, doi: 10.1016/0924-4247(93)80132-Z.

[66] A. K. Kulkarni and L. C. Chang, "Electrical and structural characteristics of chromium thin films deposited on glass and alumina substrates," *Thin Solid Films*, vol. 301, nos. 1–2, pp. 17–22, Jun. 1997, doi: 10.1016/S0040-6090(96)09553-3.

[67] *Product Datasheet Argon 5.0*, Linde Gas GmbH, Stadl-Paura, Germany, Accessed: Jun. 13, 2024. [Online]. Available: https://www.linde-gas.de/shop/de/de-ig/argon-50-argon-5-0

[68] J. Mougin, N. Rosman, G. Lucazeau, and A. Galerie, "In situ Raman monitoring of chromium oxide scale growth for stress determination," *J. Raman Spectrosc.*, vol. 32, no. 9, pp. 739–744, Sep. 2001, doi: 10.1002/jrs.734.

[69] X. Y. Zhang and D. Gall, "CrN electronic structure and vibrational modes: An optical analysis," *Phys. Rev. B, Condens. Matter*, vol. 82, no. 4, pp. 1–9, Jul. 2010, doi: 10.1103/physrevb.82.045116.

[70] M. J. Cordill, A. Taylor, J. Schalko, and G. Dehm, "Fracture and delamination of chromium thin films on polymer substrates," *Metall. Mater. Trans. A*, vol. 41, no. 4, pp. 870–875, Apr. 2010, doi: 10.1007/s11661-009-9988-9.

[71] G. Witt, "The electromechanical properties of thin films and the thin film strain gauge," *Thin Solid Films*, vol. 22, no. 2, pp. 133–156, Jun. 1974, doi: 10.1016/0040-6090(74)90001-7.

[72] H. Nakai, K. Fudaba, K. Shinzawa, and M. Hashimoto, "Electrical property on copper thin film with chromium under-layer," *Thin Solid Films*, vol. 317, nos. 1–2, pp. 202–205, Apr. 1998, doi: 10.1016/S0040-6090(97)00620-2.

[73] V. V. R. N. Rao, S. Mohan, and P. J. Reddy, "Electrical resistivity, TCR and thermoelectric power of annealed thin copper films," *J. Phys. D, Appl. Phys.*, vol. 9, no. 1, pp. 89–94, 1976, doi: 10.1088/0022-3727/9/1/015.

[74] R. Djugum and K. I. Jolic, "A fabrication process for vacuum-deposited strain gauges on thermally sprayed Al_2O_3," *J. Micromech. Microeng.*, vol. 16, no. 2, pp. 457–462, Feb. 2006, doi: 10.1088/0960-1317/16/2/032.

[75] B. C. Johnson, "Electrical resistivity of copper and nickel thin-film interconnections," *J. Appl. Phys.*, vol. 67, pp. 3018–3024, Jul. 1990, doi: 10.1063/1.345424.

[76] A. R. Patel, G. K. Shivakumar, N. C. Pandya, and N. C. Chourasia, "Temperature coefficient of the resistance of chromium-copper allow films," *Mater. Lett.*, vol. 1, nos. 5–6, pp. 181–183, 1983, doi: 10.1016/0167-577X(83)90013-7.

[77] O. Suttmann, J. F. Duesing, J. Koch, U. Stute, and L. Overmeyer, "Patterning and trimming of thin film strain sensors," in *Proc. 13th Int. Conf. Eur. Soc. Precis. Eng. Nanotechnol. (EUSPEN)*, vol. 2, 2013, pp. 340–343. [Online]. Available: https://www.euspen.eu/knowledge-base/ICE13453.pdf

[78] J. F. Düsing, J. Koch, O. Suttmann, and L. Overmeyer, "Closed-loop process control for laser patterning of thin film strain sensors," *Proc. Technol.*, vol. 26, pp. 113–119, 2016, doi: 10.1016/j.protcy.2016.08.016.

[79] K. Hoffmann, *Applying the Wheatstone Bridge Circuit*. Darmstadt, Germany: Hottinger Baldwin Messtechnik GmbH, 2022. [Online]. Available: http://eln.teilam.gr/sites/default/files/Wheatstone%20bridge.pdf

Rico Ottermann was born in Hanover, Germany, in 1993. He received the B.Sc. and M.Sc. degrees in nanotechnology from Leibniz University Hannover, Hanover, in 2018.

From then on, he began his career as a Research Assistant at the Institute of Micro Production Technology (IMPT), Leibniz University Hannover, Garbsen, Germany. Since 2021, he has led the Industry-Related Sensors Research Group until he became the Head of the Micro and Nano Integration Department in 2023. He is the author of more than 15 publications in the field of thin-film strain and temperature sensors as well as assembly and connection technology.

Dennis Kowalke received the B.Eng. degree in production engineering and the M.Sc. degree in production and management from the OWL University of Applied Sciences and Arts, Lemgo, Germany, in 2019 and 2021, respectively. He is currently pursuing the Ph.D. degree in mechanical engineering with Leibniz University Hannover, Garbsen, Germany.

His research interests include the development of structure-integrated sensors for machine tools.

Berend Denkena received the Ph.D. degree in mechanical engineering from Leibniz University Hannover, Hanover, Germany, in 1992.

Since 2001, he has been the Executive Director of the Institute of Production Engineering and Machine Tools (IFW), Leibniz University Hannover, Garbsen, Germany. His research interests include manufacturing processes, machine tools and controls, and production systems.

Dr. Denkena has been a member and a Fellow of the International Academy of Production Engineering (CIRP) since 2003 and 2007, respectively. From 2018 to 2019, he served as the President of German Academic Society of Production Technology (WGP).

Michael Korbacher was born in Schweinfurt, Bavaria, Germany, in 1989. He received the B.Eng. degree in mechanical engineering from Duale Hochschule Baden-Württemberg (DHBW) Mosbach, Mosbach, Germany in 2012 and the M.Eng. degree in mechanical engineering from Technische Hochschule (TH) Ingolstadt, Ingolstadt, Germany, in 2013.

Since 2013, he has been working with the Research and Development Department, Bosch Rexroth AG, Schweinfurt, for profiled rail systems, screw assemblies, and integrated measuring systems.

Matthias Müller was born in Marl, North Rhine-Westphalia, Germany, in 1985. He received the Bachelor of Engineering (B.Eng.) degree in mechanical engineering from the University of Bochum, Bochum, Germany, in 2013. His final thesis was on a cost-effective upgrade of existing machine tools for friction stir welding and was successfully launched on the market.

Since 2013, he has been working with the Research and Development Department, Fooke GmbH, Borken, Germany, where he became the Head of the Department in 2018.

Marc Christopher Wurz was born in Gehrden, Germany, in 1974. He received the Diploma degree in construction engineering and the Dr.-Ing. degree in mechanical engineering from Leibniz University Hannover, Hanover, Germany, in 2002 and 2009, respectively.

In 2003, he began his career as a Research Assistant at the Institute of Micro Production Technology (IMPT), Leibniz University Hannover, Garbsen, Germany, where he led the Thin-Films Research Group until he was promoted to a Senior Engineer in 2005. He has served as the Deputy Director of IMPT, Leibniz University Hannover, until 2021. He then accepted a position as a Professor at the University of Ulm, Ulm, Germany, where he led the Department of Integration of Micro and Nano Systems, German Aerospace Center (DLR). In 2022, he returned to Leibniz University Hannover to serve as the Leader of IMPT. His research interests address a wide range of micro production technology aspects, including magnetics, micro tribology, system integration, thin-film sensors, optics, and especially the manufacturing and miniaturization of quantum technological systems.

Prof. Wurz is a member of the Clusters of Excellence PhoenixD and QuantumFrontiers. On top of that, he is a Board Member of Hannover Centre for Production Technology (PZH) and the Laboratory of Nano and Quantum Engineering (LNQE). He is also an Expert of German Research Foundation (DFG) and reviews articles for IEEE journals and conferences such as European Symposium on Reliability of Electron Devices, Failure Physics and Analysis (ESREF).